

Light deflection and shadow cast by rotating Kalb-Ramond black holes

Rahul Kumar^{a,*}, Sushant G. Ghosh^{a,b,†} and Anzhong Wang^{c,d,‡}

^a Centre for Theoretical Physics, Jamia Millia Islamia, New Delhi 110025, India

^b Astrophysics and Cosmology Research Unit, School of Mathematics,
Statistics and Computer Science, University of KwaZulu-Natal,
Private Bag 54001, Durban 4000, South Africa and

^c GCAP-CASPER, Physics Department, Baylor University, Waco, Texas 76798-7316, USA

^d Institute for Theoretical Physics and Cosmology,
Zhejiang University of Technology, Hangzhou, 310032, China

(Dated: December 21, 2024)

The non-minimal coupling of the non-zero vacuum expectation value of the self-interacting antisymmetric Kalb-Ramond field with the gravity, yielding the spontaneous Lorentz symmetry breaking, leads to the power-law hairy black hole having a parameter s , which encompasses the Reissner-Nordstrom black hole ($s = 1$). We obtain the axially symmetric counterpart of this hairy solution, namely, rotating Kalb-Ramond black hole which encompasses, as special cases, Kerr ($s = 0$) and Kerr-Newman ($s = 1$) black holes. Interestingly, for a set of parameters, there exists a critical value of the Kalb-Ramond parameter ($s = s_e$), which corresponds to an extremal black hole with degenerate horizons, while for $s < s_e$, it describes a non-extremal black hole with Cauchy and event horizons, and no black hole for $s > s_e$. We find that the extremal value s_e is also influenced by these parameters. The apparent size of shadow decreases monotonically and gets more distorted with an increasing s . We investigate the effect of the Kalb-Ramond field on the rotating black hole spacetime geometry and analytically deduced corrections in the light deflection angle, which turns out to be smaller than those for the Kerr and Schwarzschild black holes. The deflection angle for Sgr A* and the shadow caused by the supermassive black hole M87* are included and compared with analogous results of Kerr black holes.

PACS numbers:

I. INTRODUCTION

The Kalb-Ramond field [1] appears as a self-interacting second rank antisymmetric tensor field in the heterotic string theory and attributed as the closed string excitation. The non-minimal coupling of the non-zero vacuum expectation value of the tensor field with the gravity sector stem to the spontaneous Lorentz symmetry violation: the ground state of a physical quantum system is characterized by non-trivial vacuum expectation values [2, 3]. It is found that the presence of Kalb-Ramond field leads to many interesting implications, namely the derived third rank antisymmetric tensor can act as a spacetime torsion [4], topological defects lead to the intrinsic angular momentum to the structures in galaxies [5], affects the observed anisotropy in the cosmic microwave background [6], provide crucial insights in the leptogenesis [7] and so on. The Kalb-Ramond field has been studied widely in the context of gravity and particle physics [8, 9]. The compelling resemblance of the Kalb-Ramond field with the spacetime torsion ascertains that the Einstein gravity with the Kalb-Ramond field as a source is equivalent to a modified theory of gravity incorporating the spacetime torsion.

The solar system based test, employed to test general relativity, reveal that the change incurred in the bending of light/perihelion precession of Mercury due to the presence of the Kalb-Ramond field would produce very tiny effects incompetent to be detected with the present-day precision [10]. However, the possibilities of detection in the quasars or black hole spacetimes, where the spacetime curvature effects are strong, are still open and will have far-reaching consequences [11].

The Kalb-Ramond field can be considered as a generalization of the electromagnetic potential with two indices, such that the gauge potential A_μ is replaced by the second rank antisymmetric tensor field $B_{\mu\nu}$ associated with the gauge-invariant rank-3 antisymmetric field strength $H_{\alpha\mu\nu}$ viz., $H_{\alpha\mu\nu} = \partial_{[\alpha} B_{\mu\nu]}$; $H_{\alpha\mu\nu}$ is analogous to the Faraday field tensor $F_{\mu\nu}$ [1]. The Einstein-Hilbert action non-minimally coupled with the self-interacting Kalb-Ramond field reads [2]

$$S = \int \sqrt{-g} d^4x \left(\frac{R}{16\pi G} - \frac{1}{12} H_{\alpha\mu\nu} H^{\alpha\mu\nu} - V(B_{\mu\nu} B^{\mu\nu} \pm b_{\mu\nu} b^{\mu\nu}) + \frac{1}{16\pi G} (\xi_2 B^{\mu\lambda} B_{\lambda}^{\nu} R_{\mu\nu} + \xi_3 B_{\mu\nu} B^{\mu\nu} R) \right) \quad (1)$$

where R and $R_{\mu\nu}$ are, respectively, the Ricci scalar and Ricci tensor and $\xi_{2,3}$ are the non-minimal coupling constants. The potential term V drives the development of a nonzero vacuum expectation value for the tensor field, i.e., $\langle B_{\mu\nu} \rangle = b_{\mu\nu}$, which breaks local Lorentz and diffeomorphism symmetry. The static spherically symmetric solution of the modified Einstein equations

*Electronic address: rahul.phy3@gmail.com

†Electronic address: sghosh2@jmi.ac.in, sghosh@gmail.com

‡Electronic address: anzhong_wang@baylor.edu

leads to the hairy black hole solution [12]

$$ds^2 = - \left(1 - \frac{2M}{r} + \frac{\Gamma}{r^{\frac{2}{s}}} \right) dt^2 + \frac{1}{\left(1 - \frac{2M}{r} + \frac{\Gamma}{r^{\frac{2}{s}}} \right)} dr^2 + r^2 d\theta^2 + r^2 \sin^2 \theta d\phi^2. \quad (2)$$

Here, M is the black hole mass, Γ and s are the spontaneous Lorentz violating parameters related to the vacuum expectation value of the Kalb-Ramond field and the non-minimal coupling parameters viz., $s = |b^2|\xi_2$ with $b^2 = b_{\mu\nu}b^{\mu\nu}$. The power-law hairy black hole (2) encompasses Schwarzschild solution when $s = 0$, Schwarzschild de-Sitter for $s = -1$, and when $s = 1$ it resembles to the Reissner-Nordstrom black hole. However, the non-rotating black hole can not be tested by observations as black hole spin is crucial for the astrophysical processes. The Kerr metric [13] is one of the important solutions of general relativity which represents a rotating black hole that can result from the gravitational collapse. This prompted us to seek axisymmetric generalization of the metric (2) or finding a Kerr-like metric, namely a rotating Kalb-Ramond metric, and to test it with the astrophysical observations. We discuss the various black hole properties including the horizons structure, the static limit surfaces, calculate the corresponding conserved quantities and establish the Smarr formula. We probe the Kalb-Ramond field signatures in the black hole spacetimes considering the available astrophysical observations. Then, we study the photon motion in the rotating Kalb-Ramond black hole spacetime, as they play crucial roles in determining the strong gravitational field features, such as gravitational lensing and shadow. Further, the Gauss-Bonnet theorem is utilized to elaborately discuss the gravitational lensing of light and analytically calculate the deflection angle in the weak field limit caused by the rotating Kalb-Ramond black hole, considering source and observer at the finite distances from the black hole. The correction in the deflection angle due to the presence of the Kalb-Ramond field for the supermassive black hole Sgr A* at the galactic center is estimated and found to be within the resolution of today's observational facilities. Moreover, the recent observation of the M87* black hole shadow by the Event Horizon Telescope (EHT) Collaboration has facilitated direct probing of the near horizon regime and offers unprecedented opportunity to test the nature of strong gravity [14, 15]. We examine the viability of the obtained rotating black hole in attributing the observed asymmetry in the M87* black hole emission ring.

The organization of this paper is as follows. We begin in Sect. II with the construction of the rotating counterpart of the metric (2), namely the rotating Kalb-Ramond metric. We also discuss generic features of the black hole including horizon structures and static limit surfaces. In Sect. III, we exploit the spacetime isometries to deduce the conserved mass and angular momentum of the rotating Kalb-Ramond black hole. The discussion of black hole shadow and the effect of

the Kalb-Ramond field on the shape and size of shadows are subjects of Sect. IV. In Sect. V, we set the premises for the gravitational deflection of light in the stationary spacetime and estimate the correction in the deflection angle owing to the Kalb-Ramond field. Finally, we summarize our main findings in Sect. VI.

II. ROTATING BLACK HOLE

Here, we find stationary and axisymmetric counterpart of the spherically symmetric solution (2) governed by four parameters M , Γ , a and a free parameter s (Kalb-Ramond Parameter) that measures potential deviation from the Kerr solution [13] and also generalizes the Kerr-Newman solution [16], which in the Boyer-Lindquist coordinates reads

$$ds^2 = - \left(\frac{\Delta - a^2 \sin^2 \theta}{\Sigma} \right) dt^2 + \frac{\Sigma}{\Delta} dr^2 - 2a \sin^2 \theta \left(1 - \frac{\Delta - a^2 \sin^2 \theta}{\Sigma} \right) dt d\phi + \Sigma d\theta^2 + \sin^2 \theta \left[\Sigma + a^2 \sin^2 \theta \left(2 - \frac{\Delta - a^2 \sin^2 \theta}{\Sigma} \right) \right] d\phi^2 \quad (3)$$

with

$$\Delta = r^2 + a^2 - 2Mr + \frac{\Gamma}{r^{-2(s-1)/s}}, \quad \Sigma = r^2 + a^2 \cos^2 \theta, \quad (4)$$

and a is the spin parameter. The metric Eq. (3) reverts to Kerr black holes as the special case $s \rightarrow 0$, to Kerr-Newman black holes for $s = 1$, and to spherically symmetric black holes (2) when only ($a = 0$). For definiteness, we call the four parameters metrics (3) as rotating Kalb-Ramond black holes, which contain all known stationary black holes of general relativity. Interestingly, like the Kerr spacetime, the rotating Kalb-Ramond black hole spacetime metric (3) still possesses the time-translational and rotational invariance isometries, which, respectively, entail the existence of two Killing vector fields $\eta_{(t)}^\mu = \left(\frac{\partial}{\partial t} \right)^\mu$ and $\eta_{(\phi)}^\mu = \left(\frac{\partial}{\partial \phi} \right)^\mu$.

The event horizon is a null stationary surface, characterized by the zero expansion for congruence of outgoing null geodesics orthogonal to the surface [17, 18]. The outward normal to such surfaces is proportional to $\partial_\mu r$, therefore, horizons are defined by the surfaces $g^{\mu\nu} \partial_\mu r \partial_\nu r = g^{rr} = \Delta = 0$, and thus their radii are zeros of

$$r^2 + a^2 - 2Mr + \frac{\Gamma}{r^{-2(s-1)/s}} = 0. \quad (5)$$

For the special case $s = 1$, Eq. (5) reduces to

$$r^2 + a^2 - 2Mr + Q^2 = 0, \quad (6)$$

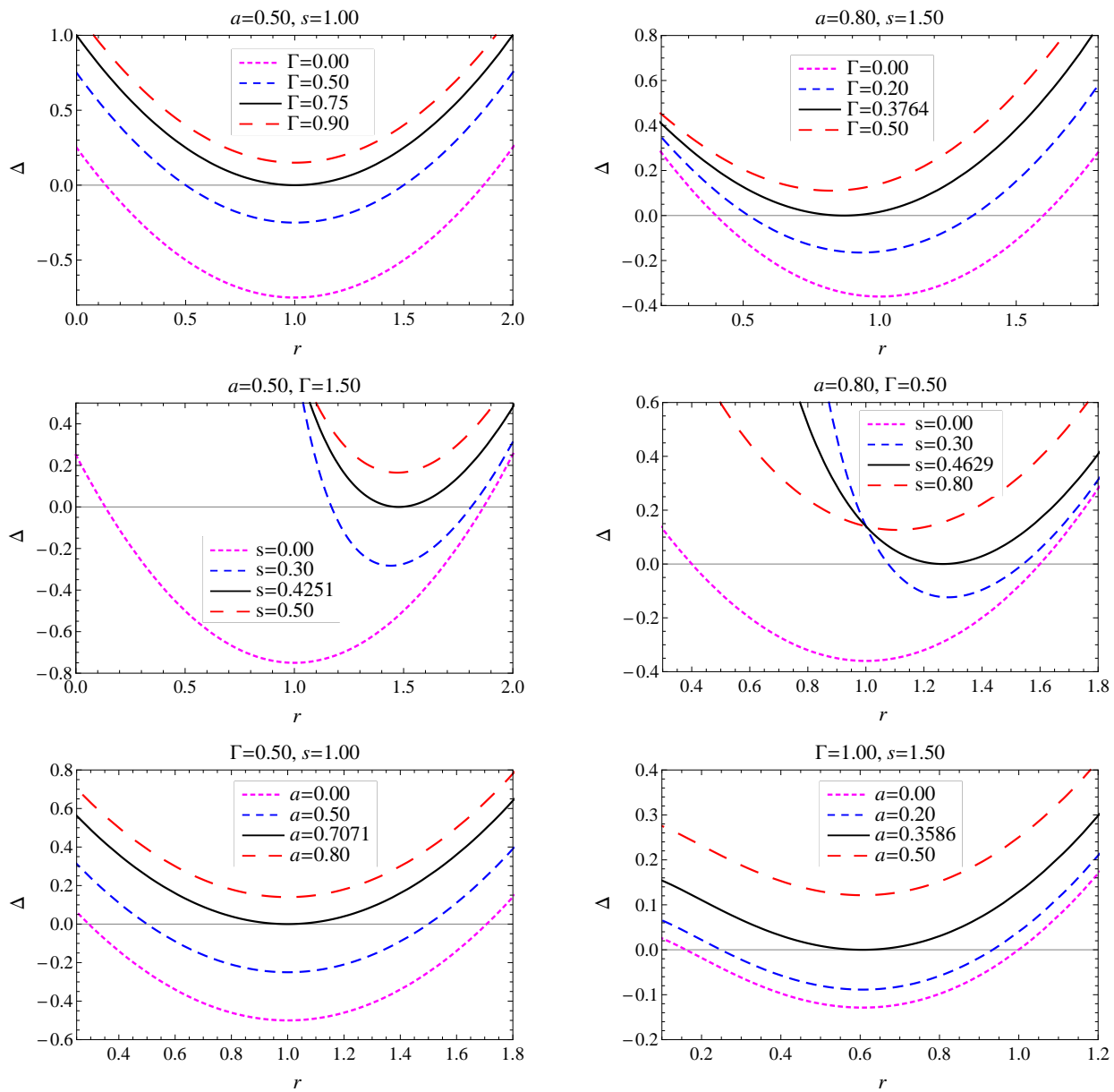


FIG. 1: The behavior of horizons with varying black hole parameters a , Γ and s . Black solid line corresponds to the extremal black hole with degenerate horizons.

where Γ is identified as the charge Q^2 , and solutions of above equation give radii of horizons for the Kerr-Newman black hole given by

$$r_{\pm} = M \pm \sqrt{M^2 - a^2 - Q^2}. \quad (7)$$

A numerical analysis of Eq. (5) reveals that it has maximum two real positive roots, corresponding to the inner Cauchy horizon (r_-) and outer event horizon (r_+), such that $r_- \leq r_+$ (cf. Fig. 1). Two distinct real positive roots of $\Delta = 0$ infers the nonextremal black hole, while no black hole in the absence of real positive roots of Eq. (5), i.e., no horizon exists. There exist particular value of parameter, $s = s_e$, for which an extremal black

hole occurs, such that Eq. (5) admits double root, i.e., when the two horizons coincide $r_- = r_+ = r_e$. We have explicitly shown that for fixed values of a and Γ , r_+ decreases and r_- increases with increasing s and eventually coincide for the extremal value of s , i.e., $r_- = r_+ = r_e$ for $s = s_e$ (cf. Fig. 1). Horizon radii vary in a similar way with increasing a and Γ . Moreover, the numerical analysis infers that it is possible to find extremal values of parameters $a = a_e$ for fixed s and Γ , and $\Gamma = \Gamma_e$ for fixed a and s , for which algebraic equation $\Delta = 0$ has double roots as depicted in Fig. 1. Figure 1 also shows that for the fixed values of M and a , the event horizon radii for the rotating Kalb-Ramond

black hole are smaller as compared to those for the Kerr black hole.

The static observers in the stationary spacetime follow the worldline of timelike Killing vector $\eta_{(t)}^\mu$, such that their four-velocity is $u^\mu \propto \eta_{(t)}^\mu$ with the proper normalization factor. These observers can exist as long as $\eta_{(t)}^\mu$ is time-like, such that $\eta_{(t)}^\mu \eta_{\mu(t)} = g_{tt} = 0$ or

$$r^2 + a^2 \cos^2 \theta - 2Mr + \frac{\Gamma}{r^{-2(s-1)/s}} = 0, \quad (8)$$

defines the boundary of static limit surface (SLS), which apart from black hole parameters also depends on θ and coincide with the event horizon only at the poles. For the particular case $s = 1$, Eq. (8) corresponds to the Kerr-Newman black hole as

$$r^2 + a^2 \cos^2 \theta - 2Mr + Q^2 = 0, \quad (9)$$

and admits the solutions

$$r_{SLS}^\pm = M \pm \sqrt{M^2 - a^2 \cos^2 \theta - Q^2},$$

which can be identified as the SLS radii for the Kerr-Newman black hole. Equation (8) is solved numerically and behavior of static limit surfaces is shown in Fig. 2. It is clear from Fig. 2, that radii of SLS decreases with increasing Γ and a . The two SLS, corresponding to the real positive roots of Eq. (8), get coincide for suitably chosen parameters. However, these extremal values are different from those for the degenerate horizons. For fixed values of M and a , the SLS radii for the rotating Kalb-Ramond black holes are smaller than the Kerr black hole values. Likewise the Kerr black hole, apart from $\Delta = 0$, which is merely a coordinate singularity, rotating metric (3) is also singular at $\Sigma = 0$, which attributes to a ring shape physical singularity at the equatorial plane of center of black hole with radius a .

Zero angular momentum observer (ZAMO) are the stationary observers with zero angular momentum with respect to the spatial infinity, but due to the frame dragging they have the position dependent angular velocity ω

$$\omega = \frac{d\phi}{dt} = -\frac{g_{t\phi}}{g_{\phi\phi}} = \frac{2Mar - \frac{\Gamma a}{r^{-2(s-1)/s}}}{[(r^2 + a^2)^2 - a^2 \Delta]}, \quad (10)$$

which increase as the observer approach the black hole and eventually takes the maximum value at the event horizon

$$\Omega = \omega|_{r=r_+} = \frac{2Mar_+ - \frac{\Gamma a}{r_+^{-2(s-1)/s}}}{(r_+^2 + a^2)^2}, \quad (11)$$

such that observers are in a state of corotation with the black hole. Here, Ω is the black hole angular velocity, which in the limits, $s = 0$, reads

$$\Omega = \frac{a}{r_+^2 + a^2}, \quad (12)$$

and corresponds to the Kerr black hole value [18, 19].

III. KOMAR MASS AND ANGULAR MOMENTUM

The mass and angular momentum attributed to the stationary, asymptotically flat black hole spacetime correspond to the conserved quantities associated with the asymptotically time-like and space-like Killing vectors fields, respectively, $\eta_{(t)}^\mu$ and $\eta_{(\phi)}^\mu$. Following the Komar [20] definitions of conserved quantities, we consider a spacelike hypersurface Σ_t , extending from the event horizon to the spatial infinity, which is a surface of constant t with unit normal vector n_μ [19, 21]. The two-boundary S_t of the hypersurface Σ_t is a constant t and constant r surface with unit outward normal vector σ_μ . The effective mass reads [20]

$$M_{\text{eff}} = -\frac{1}{8\pi} \int_{S_t} \nabla^\mu \eta_{(t)}^\nu dS_{\mu\nu}, \quad (13)$$

where $dS_{\mu\nu} = -2n_{[\mu}\sigma_{\nu]} \sqrt{h} d^2\theta$ is the surface element of S_t , h is the determinant of (2×2) metric on S_t and

$$n_\mu = -\frac{\delta_\mu^t}{|g^{tt}|^{1/2}}, \quad \sigma_\mu = \frac{\delta_\mu^r}{|g^{rr}|^{1/2}}, \quad (14)$$

are, respectively, timelike and spacelike unit outward normal vectors. Thus mass integral Eq. (13) turned into integral over closed 2-surface at infinity

$$\begin{aligned} M_{\text{eff}} &= \frac{1}{4\pi} \int_0^{2\phi} \int_0^\phi \frac{\sqrt{g_{\theta\theta}g_{\phi\phi}}}{|g^{tt}g^{rr}|^{1/2}} \nabla^t \eta_{(t)}^r d\theta d\phi, \\ &= \frac{1}{4\pi} \int_0^{2\phi} \int_0^\phi \frac{\sqrt{g_{\theta\theta}g_{\phi\phi}}}{|g^{tt}g^{rr}|^{1/2}} (g^{tt}\Gamma_{tt}^r + g^{t\phi}\Gamma_{t\phi}^r) d\theta d\phi. \end{aligned} \quad (15)$$

Using the metric elements Eq. (3), we obtain the effective mass of rotating Kalb-Ramond black hole

$$M_{\text{eff}} = M + \frac{1}{2ras} \left((r^2 + a^2)(s-2) \tan^{-1} \left(\frac{a}{r} \right) - ars \right) \frac{\Gamma}{r^{-\frac{s-2}{s}}}, \quad (16)$$

which is clearly corrected due to the Kalb-Ramond field, and goes over to the Kerr black hole case that is $M_{\text{eff}} = M$, when $s = 0$. For the special case $s = 1$, Eq. (16) resembles the effective mass for the Kerr-Newman black hole with Γ as the electric charge Q^2 and reads [22]

$$M_{\text{eff}} = M - \frac{Q^2}{2r^2a} \left((r^2 + a^2) \tan^{-1} \left(\frac{a}{r} \right) + ar \right). \quad (17)$$

The effective mass for the spherically symmetric Kalb-Ramond black hole ($a = 0$) is obtained from Eq. (16) and reads

$$M_{\text{eff}} = M - \frac{1}{s} \frac{\Gamma}{r^{-\frac{s-2}{s}}},$$

which further reverts the values for the Reissner-Nordstrom black hole as a special case $s = 1$

$$M_{\text{eff}} = M - \frac{Q^2}{r},$$

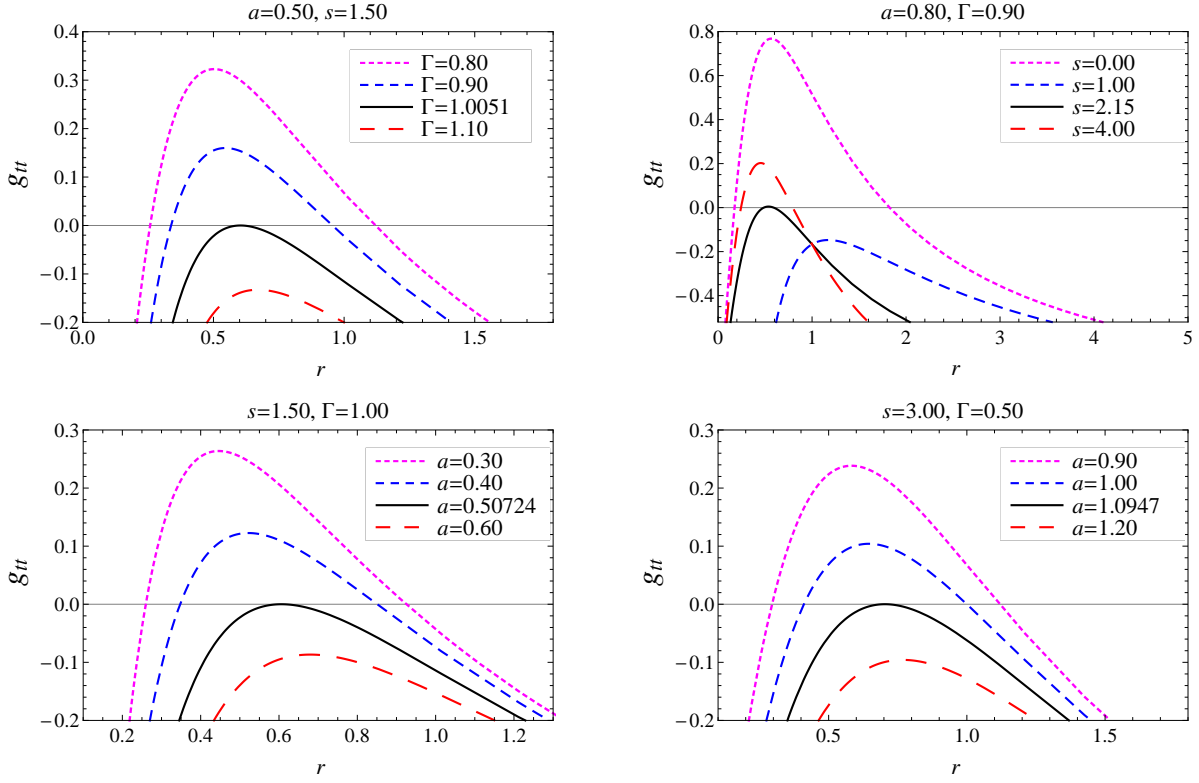


FIG. 2: The behavior of SLS with varying parameters a, Γ, s and $\theta = \pi/4$. The Black solid curve in each plot corresponds to the degenerate SLS.

and Schwarzschild black hole $M_{\text{eff}} = M$, when $s = 0$. Now, we use the spacelike Killing vector $\eta_{(\phi)}^\mu$ to calculate the effective angular momentum [20]

$$J_{\text{eff}} = \frac{1}{16\pi} \int_{S_t} \nabla^\mu \eta_{(\phi)}^\nu dS_{\mu\nu}, \quad (18)$$

using the definitions of surface element, Eq. (18) recast as

$$\begin{aligned} J_{\text{eff}} &= -\frac{1}{8\pi} \int_0^{2\phi} \int_0^\phi \nabla^\mu \eta_{(t)}^\nu n_\mu \sigma_\nu \sqrt{h} d\theta d\phi, \\ &= \frac{1}{8\pi} \int_0^{2\phi} \int_0^\phi \frac{\sqrt{g_{\theta\theta} g_{\phi\phi}}}{|g^{tt} g^{rr}|^{1/2}} (g^{tt} \Gamma_{t\phi}^r + g^{t\phi} \Gamma_{\phi\phi}^r) d\theta d\phi \end{aligned}$$

After performing the integration for the rotating Kalb-Ramond black hole Eq. (3), this reads

$$\begin{aligned} J_{\text{eff}} &= Ma + \frac{\Gamma}{4ra^2s} \frac{1}{r^{-\frac{s-2}{s}}} \left((r^2 + a^2)^2 (s-2) \tan^{-1} \left(\frac{a}{r} \right) \right. \\ &\quad \left. - ((3s-2)a^2 + r^2(s-2)) ra \right), \end{aligned} \quad (20)$$

which identically vanishes in the limiting case of $a = 0$, and for the particular case of $s = 1$ it reduces to

$$J_{\text{eff}} = Ma + \frac{\Gamma(r^2 - a^2)}{4ar} - \frac{\Gamma}{4a^2r^2} (r^2 + a^2)^2 \tan^{-1} \left(\frac{a}{r} \right), \quad (21)$$

which can be identified as the Kerr-Newman black hole value [22]. In the asymptotic limits, $r \rightarrow \infty$, the effective angular momentum Eq. (20) restore the value $J_{\text{eff}} = Ma$, which corresponds to the value for the Kerr black hole. Thus, the effects of the Kalb-Ramond field subsides at very large distance from the black hole. Equations (16) and (20) infer that at the finite radial distance the values of the effective mass and angular momentum get modified from their asymptotic values and depend on the sign of Γ . In Fig. 3, we have shown the normalized effective mass and angular momentum variation with radial distance r for various values of black hole parameters. Such that, at asymptotically large r , the normalized values become a unity, as expected. It is clear that for fixed values of a and s , the effective values of M_{eff}/M and J_{eff}/Ma decrease with increasing field parameter Γ . Whereas, for fixed values of a and Γ , the effective mass and angular momentum show diverse behavior with varying s . Moreover, outside the event horizon, the effective angular momentum of the black hole reduces with increasing Kalb-Ramond field parameter s . Thus, for the rotating Kalb-Ramond black hole, the values of effective mass and effective angular momentum are smaller as compared to those for the Kerr black hole.

Since it is well-known that the Killing vectors $\eta_{(t)}^\mu$ or $\eta_{(\phi)}^\mu$ are not the generators of the stationary black hole horizon, rather it is their specific linear combination [19]

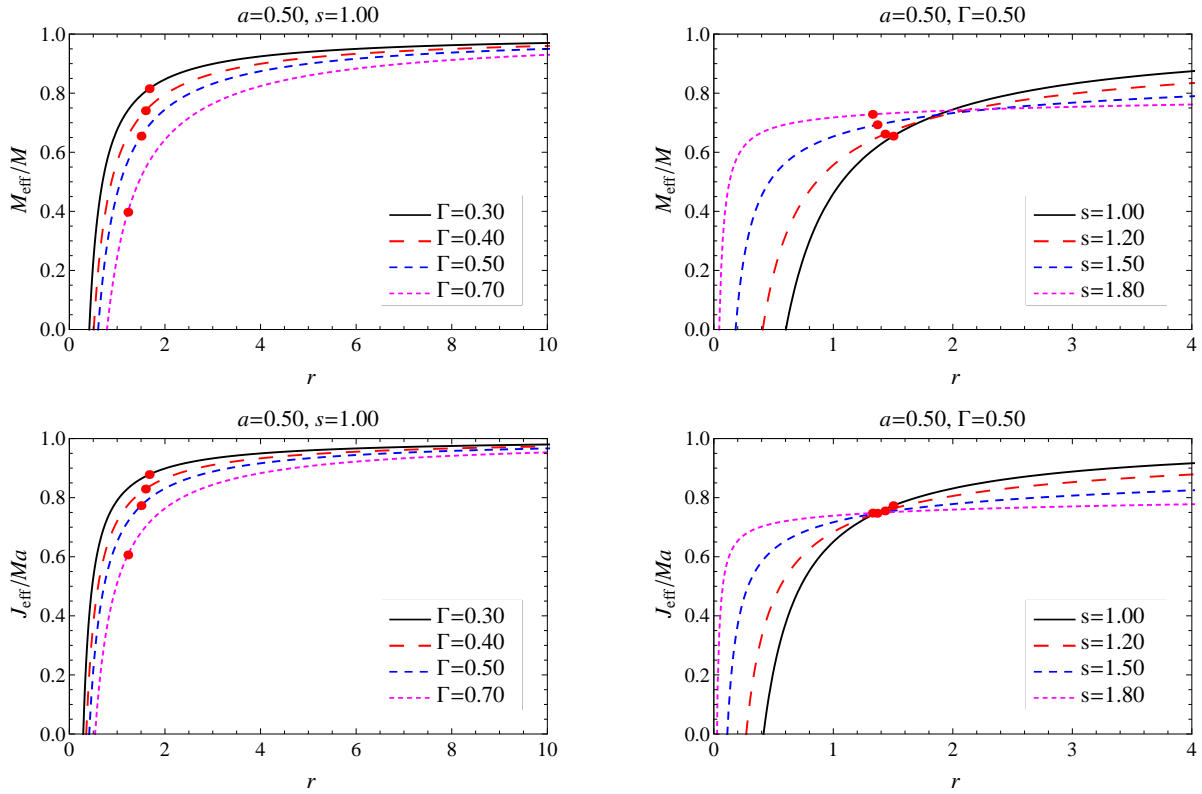


FIG. 3: The behavior of effective mass and angular momentum vs r for different values of the parameters. Black solid curves correspond to the Kerr-Newman black hole and red dots in each curve denote the locations of event horizon.

as

$$\chi^\mu = \eta_{(t)}^\mu + \Omega \eta_{(\phi)}^\mu, \quad (22)$$

such that χ^μ is globally time-like outside the event horizon, though it is Killing vector only at the horizon [19]. The Komar conserved quantity at the event horizon associated with χ^μ reads as [20]

$$\begin{aligned} J_\chi &= -\frac{1}{8\pi} \int_{S_t} \nabla^\mu \chi^\nu dS_{\mu\nu}, \\ &= -\frac{1}{8\pi} \int_{S_t} \nabla^\mu \left(\eta_{(t)}^\mu + \Omega \eta_{(\phi)}^\mu \right) dS_{\mu\nu}. \end{aligned} \quad (23)$$

Using Eqs. (16) and (20), we obtain

$$\begin{aligned} J_\chi &= M_{\text{eff}} - 2\Omega J_{\text{eff}}, \\ &= \frac{M(r_+^2 - a^2)}{(r_+^2 + a^2)} - \frac{(r_+^2 - (s-1)a^2)}{(r_+^2 + a^2)s} \frac{\Gamma}{r_+^{-(s-2)/s}} \end{aligned} \quad (24)$$

To understand the implication of the above conserved quantity, we calculate the black hole horizon temperature [19]

$$\begin{aligned} T_+ &= \frac{\kappa}{2\pi} = \frac{\Delta'}{4\pi(r_+^2 + a^2)}, \\ &= \frac{(r_+ - M)}{2\pi(r_+^2 + a^2)} + \frac{(s-1)}{2\pi s(r_+^2 + a^2)} \frac{\Gamma}{r_+^{-(s-2)/s}}. \end{aligned} \quad (25)$$

Whereas entropy is defined as follow

$$S_+ = \frac{A}{4} = \pi(r_+^2 + a^2). \quad (26)$$

Equations (24), (25) and (26) clearly infer that

$$J_\chi = M_{\text{eff}} - 2\Omega J_{\text{eff}} = 2S_+ T_+. \quad (27)$$

Therefore, the Komar conserved quantity corresponding to the null Killing vector at the event horizon χ^μ is twice the product of the black hole entropy and the horizon temperature and hence satisfy the Smarr formula [23, 24].

IV. BLACK HOLE SHADOW

The light originating either from the luminous background or the accretion disk surrounding the black hole arrives in the vicinity of the event horizon, and a part of it gets trapped inside the horizon while another part escapes to infinity. This results in the optical appearance of the black hole, namely the black hole shadow encircled by the bright photon ring [25–28]. Synge [25] in the pioneering work, calculated the shadow cast by a Schwarzschild black hole, and thereafter Bardeen [27] studied the shadow of Kerr black holes. In the past decade, shadows have been extensively studied

for varieties of black holes [29, 30]. Interestingly, it is found that photon emission ring, the light rays that orbit around the black hole many times before they reach the distant observer, explicitly depends on the spacetime geometry while largely remains independent of the astrophysical details of accretion flow models [31–33]. Thus the structure of the photon ring encompassing the black hole shadow is a potential tool to testifies the signatures of strong gravitational lensing of nearby radiation and hence its shape and size can reveal valuable information regarding the near-horizon field features of gravity.

For this purpose, we study the motion of test particle in a stationary and axially symmetric black hole spacetime, which neglecting the back reaction is completely defined by the four integral of motions: the particle rest mass m_0 , total energy \mathcal{E} , axial angular momentum \mathcal{L} and the Carter constant \mathcal{Q} , related to the latitudinal motion of the test particle [34]. Using these integrals of motion, we obtained the null geodesics equation of motion in the first-order differential form [19, 34]

$$\Sigma \frac{dt}{d\tau} = \frac{r^2 + a^2}{\Delta} (\mathcal{E}(r^2 + a^2) - a\mathcal{L}) - a(a\mathcal{E} \sin^2 \theta - \mathcal{L}) \quad (28)$$

$$\Sigma \frac{dr}{d\tau} = \pm \sqrt{\mathcal{R}(r)}, \quad (29)$$

$$\Sigma \frac{d\theta}{d\tau} = \pm \sqrt{\Theta(\theta)}, \quad (30)$$

$$\Sigma \frac{d\phi}{d\tau} = \frac{a}{\Delta} (\mathcal{E}(r^2 + a^2) - a\mathcal{L}) - \left(a\mathcal{E} - \frac{\mathcal{L}}{\sin^2 \theta} \right), \quad (31)$$

where τ is the affine parameter along the geodesics and

$$\mathcal{R}(r) = ((r^2 + a^2)\mathcal{E} - a\mathcal{L})^2 - \Delta((a\mathcal{E} - \mathcal{L})^2 + \mathcal{K}), \quad (32)$$

$$\Theta(\theta) = \mathcal{K} - \left(\frac{\mathcal{L}^2}{\sin^2 \theta} - a^2 \mathcal{E}^2 \right) \cos^2 \theta, \quad (33)$$

\mathcal{K} stands for the separable constant which is related with the Carter's constant of motion $\mathcal{Q} = \mathcal{K} + (a\mathcal{E} - \mathcal{L})^2$ [19, 34]. For $\mathcal{K} = 0$, photon motions are restricted only to the equatorial plane. $\mathcal{R}(r)$ and $\Theta(\theta)$ are related to the effective potentials for the radial and the latitudinal motion of the photon. Such that zeros of these potential determine the turning point in the photon trajectories. Let define the dimensionless impact parameters

$$\eta \equiv \mathcal{K}/\mathcal{E}^2, \quad \xi \equiv \mathcal{L}/\mathcal{E}, \quad (34)$$

which characterize the null geodesics. Such that, depending upon their values photons may undergo scattering ($\eta > \eta_c$), capturing ($\eta < \eta_c$) and unstable orbits ($\eta = \eta_c$), which are very crucial for the shadow formation and indeed mark the shadow silhouette. Thus on the observer's celestial sky, the scattered photons account for the bright region, whereas captured photons attribute to the dark region. These unstable photon orbits, of constant radii r_p , witness continuum radial turning points, i.e. $\dot{r}_p = \ddot{r}_p = 0$ corresponding to the

extrema of effective potential

$$\mathcal{R}|_{(r=r_p)} = \frac{\partial \mathcal{R}}{\partial r} \Big|_{(r=r_p)} = 0 \quad \text{and} \quad \frac{\partial^2 \mathcal{R}}{\partial r^2} \Big|_{(r=r_p)} > 0, \quad (35)$$

and form a photon region around the black hole. Further, due to rotation of the black hole, photons can either have prograde motion or the retrograde motion, whose respective radii r_p^- and r_p^+ can be obtained as zeros of $\eta_c = 0$. For the Kerr black hole, the photon orbit radii r_p are

$$\begin{aligned} r_p^- &= 2M \left[1 + \cos \left(\frac{2}{3} \cos^{-1} \left[-\frac{|a|}{M} \right] \right) \right], \\ r_p^+ &= 2M \left[1 + \cos \left(\frac{2}{3} \cos^{-1} \left[\frac{|a|}{M} \right] \right) \right], \end{aligned} \quad (36)$$

which for the Schwarzschild black hole ($a = 0$), takes the degenerate value $r_p^- = r_p^+ = 3M$. For the visualization of the black hole shadow, one has to consider the projection of the photon region into the image plane. The locus of the shadow boundary is defined in terms of two celestial coordinates α and β which by construction lie in the celestial plane perpendicular to the line joining the observer and the center of the black hole, and are related to the photon four-momentum $p^{(\mu)}$ measured in the orthonormal-tetrad basis [27]. For an observer at position (r_o, θ_o) , in the far exterior region of the black hole, they read [28]

$$\alpha = -r_o \frac{p^{(\phi)}}{p^{(t)}}, \quad \beta = r_o \frac{p^{(\theta)}}{p^{(t)}}. \quad (37)$$

On using geodesic Eqs. (28), (30) and (31), the celestial coordinates yield

$$\begin{aligned} \alpha &= -r_o \frac{\xi_c}{\sqrt{g_{\phi\phi}(\zeta - \gamma\xi_c)}} \Big|_{(r_o, \theta_o)}, \\ \beta &= \pm r_o \frac{\sqrt{\Theta_\theta(\theta)}}{\sqrt{g_{\theta\theta}(\zeta - \gamma\xi_c)}} \Big|_{(r_o, \theta_o)}, \end{aligned} \quad (38)$$

with

$$\zeta = \sqrt{\frac{g_{\phi\phi}}{g_{t\phi}^2 - g_{tt}g_{\phi\phi}}}, \quad \gamma = -\frac{g_{t\phi}}{g_{\phi\phi}}\zeta. \quad (39)$$

For an observer sitting in the asymptotically flat region ($r_o \rightarrow \infty$), the celestial coordinates Eq. (38) can be simplified as [27, 28]

$$\alpha = -\xi_c \csc \theta_o, \quad \beta = \pm \sqrt{\eta_c + a^2 \cos^2 \theta_o - \xi_c^2 \cot^2 \theta_o}. \quad (40)$$

We further consider that the observer is perceiving black hole at an inclination angle $\theta_o = \pi/2$. Using geodesic Eqs. (31)–(29) and celestial coordinate (38), we obtain

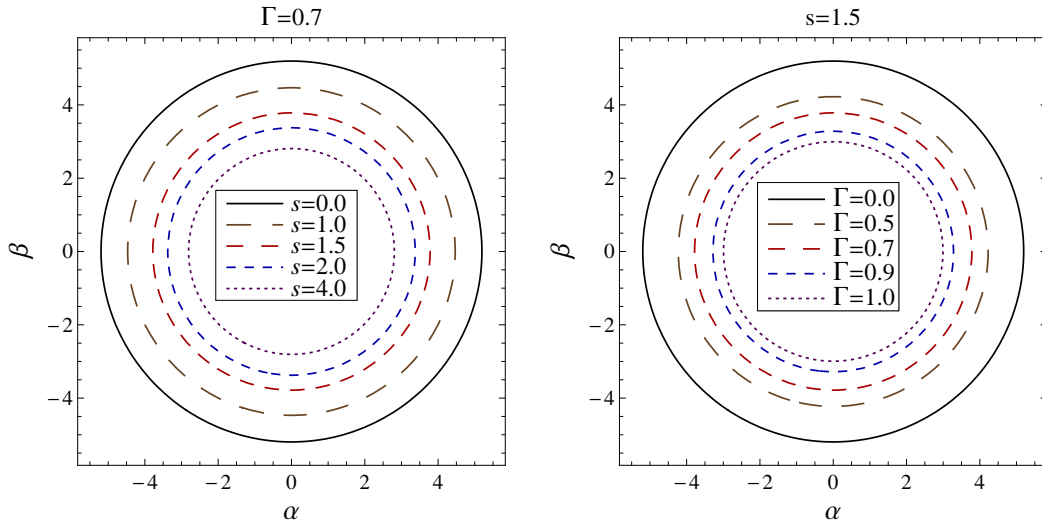


FIG. 4: Non-rotating Kalb-Ramond black hole shadows with varying parameters. Black solid line corresponds to the Schwarzschild black hole shadow.

$$\alpha = \frac{1}{a^2[m(r_p) + r_p(-1 + m'(r_p))]^2} \left[r_p^3(-r_p^3 + m(r_p)) \right. \\ \left. (4a^2 + 6r_p^2 - 9m(r_p)r_p) \right. \\ \left. - 2r_p(2a^2 + r_p^2 - 3m(r_p)r_p)m'(r_p) - r_p^3m'(r_p)^2 \right], \\ \beta = \frac{(a^2 - 3r_p^2)m(r_p) + r_p(a^2 + r_p^2)(1 + m'(r_p))}{a(m(r_p) + r_p(-1 + m'(r_p)))}, \quad (41)$$

where for brevity, we have defined

$$m(r) = M - \frac{\Gamma}{2r^{-(s-2)/s}}. \quad (42)$$

For the non-rotating case, Eq. (41) yield

$$\alpha^2 + \beta^2 = \frac{2r_p^2 \left[4r_p^2 - 12M^2 - 3\frac{\Gamma^2}{r_p^{-2(s-2)/s}} + 12M\frac{\Gamma}{r_p^{-(s-2)/s}} \right]}{(2M - \frac{\Gamma}{r_p^{-(s-2)/s}} - 2r_p)^2}, \quad (43)$$

which clearly elucidates that for static spherically symmetric Kalb-Ramond black hole metric the shadow is circular in shape. For the Schwarzschild black hole ($a = 0, s = 0, r_p = 3M$), Eq. (41) reduces to

$$\alpha^2 + \beta^2 = 27M^2, \quad (44)$$

and infer that the shadow radius is $3\sqrt{3}M$. Taking the unstable photon orbit radius r_p as a parameter, the parametric plot β vs α in Eq. (41) delineate the shadow for the rotating Kalb-Ramond black hole. Shadows of non-rotating Kalb-Ramond black holes are smaller than those for the Schwarzschild black holes, and the shadow size decrease with both increasing s and Γ . Shadows of rotating Kalb-Ramond black holes for various values of

black hole parameters are shown in Fig. 5, which clearly infer that the presence of the Kalb-Ramond field has a profound influence on the apparent shape and size of the shadow. For the characterization of shadows, we define two astronomical observables, namely shadow area A and oblateness parameter D [35, 36]

$$A = 2 \int \beta(r_p) d\alpha(r_p) = 2 \int_{r_p^-}^{r_p^+} \left(\beta(r_p) \frac{d\alpha(r_p)}{dr_p} \right) dr_p, \quad (45)$$

$$D = \frac{\alpha_r - \alpha_l}{\beta_t - \beta_b}, \quad (46)$$

where A and D , respectively, characterize the shadow size and shape. In Fig. 6, the shadow observables A and D are plotted with varying Γ for different values of s and a and it is evident that increasing Γ gradually decreases the shadow size whereas it increases the distortion (cf. Fig. 6). The variation of A and D with spin parameter a is shown in Fig. 7. Moreover, the shadows of the rotating Kalb-Ramond black hole are smaller and more distorted than the corresponding Kerr black hole shadow ($\Gamma = 0$ or $s = 0$). The black solid curve in Fig. 7 corresponds to the Kerr black hole. For the estimation of the black hole parameters, we plotted these shadow observables in the (a, Γ) planes for different values of s in Fig. 8. This is evident that each curve of constant A and D intersects at a unique point, which gives the value of black hole parameters a and Γ .

The EHT Collaboration [37] using the Very Large Baseline Interferometry technique has recently observed the central compact emission region of the galactic center of M87 at the 1.3 mm wavelength, thereby opening a new window to test gravity in the strong-field regime [14, 15]. The central flux depression by $\gtrsim 10 : 1$ and the asymmetric emission ring of crescent diameter $42 \pm 3 \mu\text{as}$

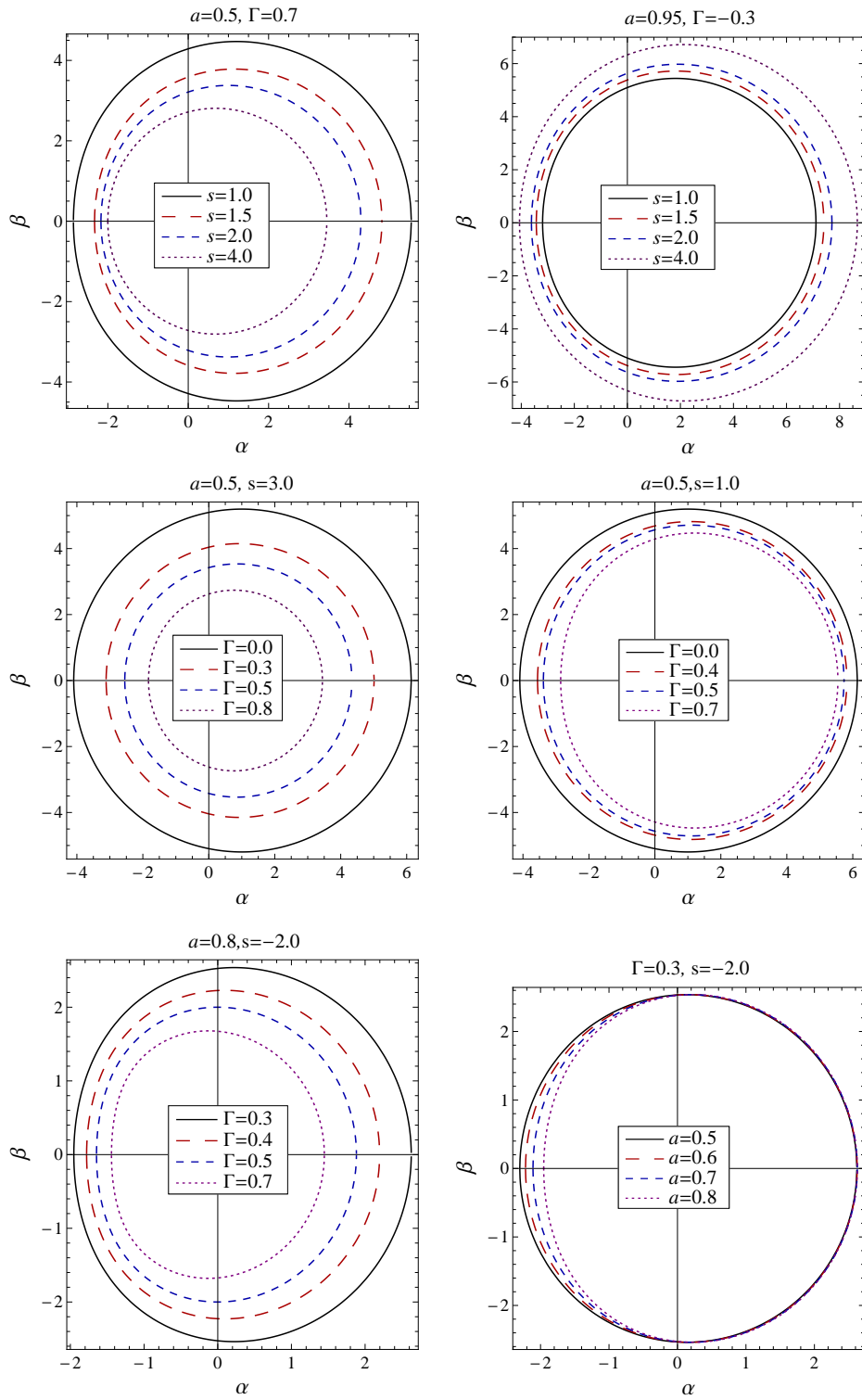


FIG. 5: Plot showing the rotating Kalb-Ramond black hole shadows with varying parameters.

in the captured image of M87* provide direct evidence of the black hole shadow, which is consistent with the predicted image of Kerr black hole in general relativity. [14, 15]. The observed shadow of M87* black hole has been used to constrain or rule out our various black hole

models in general relativity as well in modified gravities [38]. We can use the relevant shadow observable, the asymmetry parameter ΔC , to constrain the parameter space of rotating Kalb-Ramond black hole. The shadow boundary can be described by a one-dimensional closed

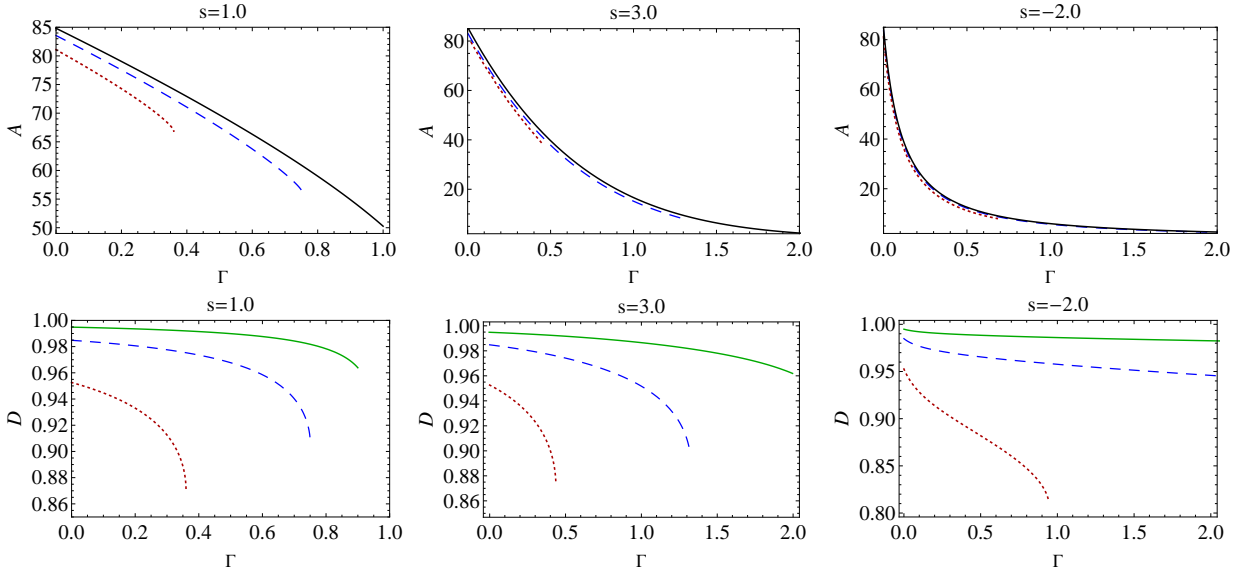


FIG. 6: The shadow area A and oblateness observables D vs Γ for the rotating Kalb-Ramond black hole, (solid Black curve) for non-rotating black hole $a = 0.0$, (solid Green curve) for $a = 0.3$, (dashed Blue curve) for $a = 0.5$, and (dotted Red curve) for $a = 0.8$.

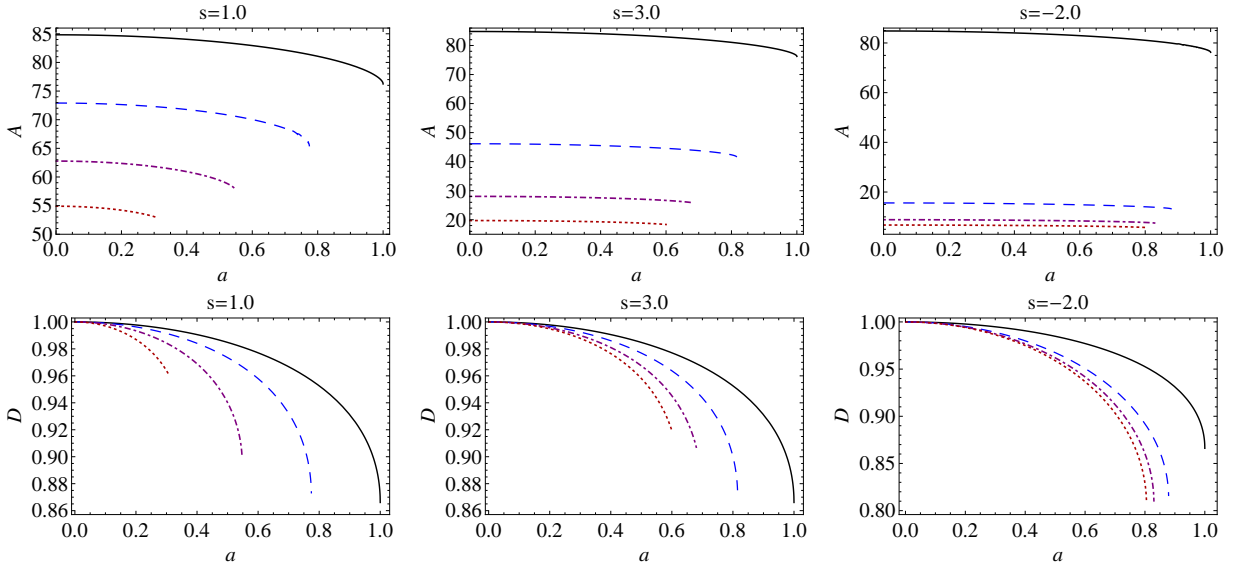


FIG. 7: The shadow area A and oblateness observables D vs a for the rotating Kalb-Ramond black hole, (solid Black curve) for the Kerr black hole $\Gamma = 0.0$, (dashed Blue curve) for $\Gamma = 0.4$, (dashdotted Magenta curve) for $\Gamma = 0.7$ and (dotted Red curve) for $\Gamma = 0.9$.

curve characterized by the radial and angular coordinates $(R(\varphi), \varphi)$ in a polar coordinate system with the origin at the shadow center (α_C, β_C) . The shadow average radius \bar{R} is defined by [32]

$$\bar{R} = \frac{1}{2\pi} \int_0^{2\pi} R(\varphi) d\varphi, \quad (47)$$

with

$$R(\varphi) = \sqrt{(\alpha - \alpha_C)^2 + (\beta - \beta_C)^2}, \quad \varphi \equiv \tan^{-1} \left(\frac{\beta}{\alpha - \alpha_C} \right).$$

The circularity deviation ΔC measures the deviation from a perfect circle and defined in terms of the root-means-square distance from the average radius [32, 33]

$$\Delta C = 2 \sqrt{\frac{1}{2\pi} \int_0^{2\pi} (R(\varphi) - \bar{R})^2 d\varphi}, \quad (48)$$

such that for a perfect circular shadow, ΔC identically vanishes. Tracing the emission ring, the EHT deduced that the circularity deviation in the observed image of the M87* black hole is $\Delta C \leq 0.10$ [14]. We calculate the

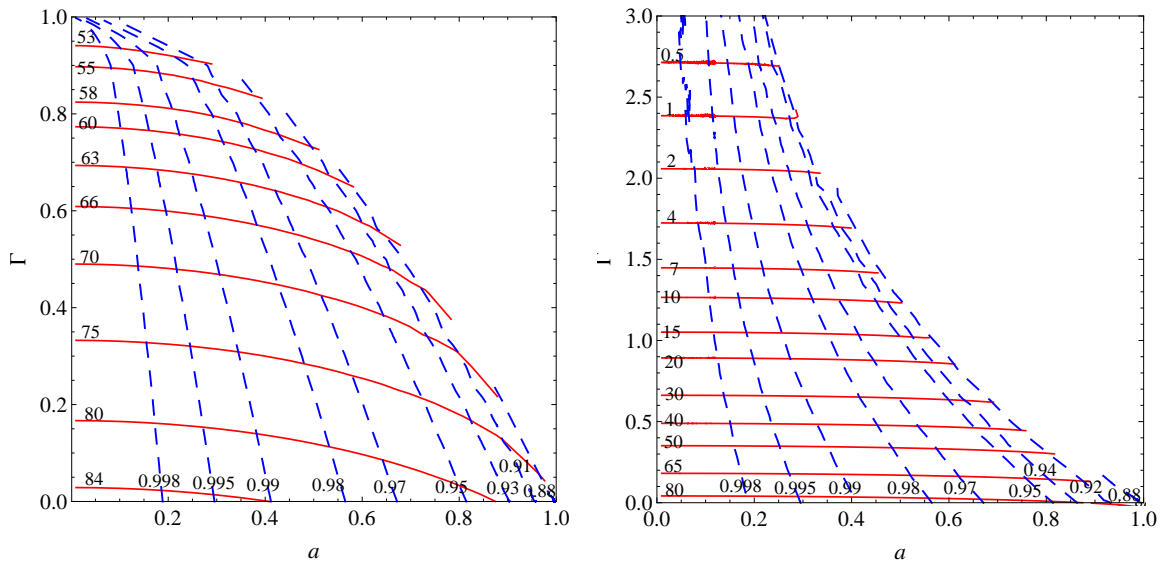


FIG. 8: Contour plots of the observables A and D in the plane (a, Γ) for the rotating Kalb-Ramond black hole (left panel) for $s = 1$ and (right panel) for $s = 3$. Each curve is labeled with the corresponding values of A and D . Solid red curves correspond to the area, and dashed blue curves for oblateness parameter.

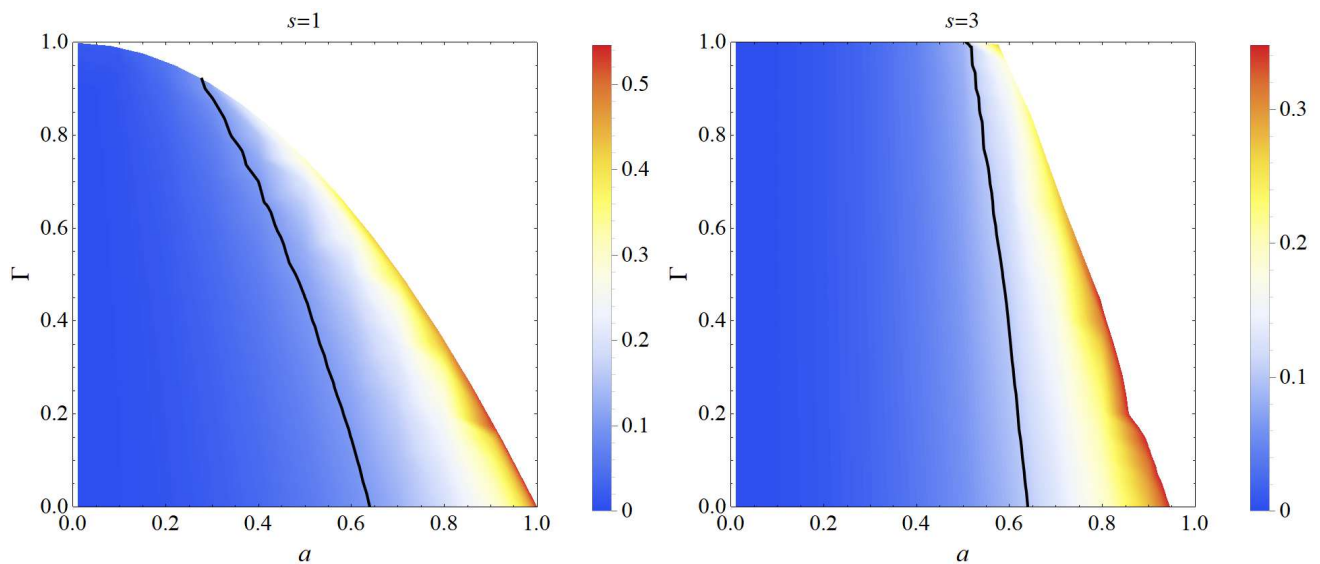


FIG. 9: Shadow asymmetry parameters ΔC as a function of (a, Γ) for the rotating Kalb-Ramond black hole. Black solid line corresponds for the $\Delta C = 0.10$.

circularity deviation for metric Eq. (3) and use the EHT bound to put constraints on the black hole and Kalb-Ramond field parameters. The interplay between spin a and field parameters Γ and s is shown in Fig 9.

V. GRAVITATIONAL DEFLECTION OF LIGHT

Gibbon and Werner [39] used the Gauss-Bonnet theorem, which connects the differential geometry of the surface with its topology, in the context of optical

geometry to calculate the deflection angle of light in a spherically symmetric black hole spacetime [40]. Later, Ishihara *et al.* [41], taking into account the finite distance from the black hole to a light source and an observer, calculate the light deflection angle in static, spherically symmetric and asymptotically flat spacetimes, which is generalized by Ono *et al.* [42] for the stationary and axisymmetric spacetimes. We follow their approach to calculate the light deflection angle in the weak-field limit caused by the rotating Kalb-Ramond black hole. We assume that both the observer (O) and

the source (S) are at the finite distance from the black hole (L) (cf. Fig. 10). The deflection angle at the equatorial plane can be defined in terms of the angle made by light rays at the source and observer Ψ_S and Ψ_O , respectively, and their angular coordinate separation Φ_{OS} [42]

$$\alpha_D = \Psi_O - \Psi_S + \Phi_{OS}. \quad (49)$$

Here, $\Phi_{OS} = \Phi_O - \Phi_S$, where Φ_O and Φ_S are, respectively, the angular coordinates of the observer and the source. We consider a 3-dimensional Riemannian manifold $(^3)\mathcal{M}$ defined by optical metric γ_{ij} , in which the photon motion is described as a spatial curve [39]. To calculate the deflection angle using Gauss-Bonnet theorem, we consider a quadrilateral $\infty\Box_S^\infty$, the domain of integration, embedded in the curved space $(^3)\mathcal{M}$ which consist of spatial light ray curve from source to the observer, a circular arc segment C_r of coordinate radius r_C ($r_C \rightarrow \infty$), and two outgoing radial lines from O and from S (cf. Fig. 10). The Gauss-Bonnet theorem yield the geometrically invariant definition as follow [42]

$$\alpha_D = - \int \int_{\infty\Box_S^\infty} K dS + \int_S^O k_g dl, \quad (50)$$

where K is the Gaussian curvature of the two-dimensional surface of light propagation, k_g is the geodesic curvature of light curves, a measure for the deviation of curve from the geodesics. dS and dl are, respectively, the infinitesimal area element of the surface and arc length element. Since Eq. (50) is invariant in differential geometry, α_D is well-defined even if focal point L is a singularity [41]. For the null geodesics $ds^2 = 0$, we get

$$dt = \pm \sqrt{\gamma_{ij} dx^i dx^j} + N_i dx^i, \quad (51)$$

with

$$\begin{aligned} \gamma_{ij} dx^i dx^j &= \frac{\Sigma^2}{\Delta(\Delta - a^2 \sin^2 \theta)} dr^2 + \frac{\Sigma^2}{\Delta - a^2 \sin^2 \theta} d\theta^2 \\ &+ \left(r^2 + a^2 + \frac{2m(r)ra^2 \sin^2 \theta}{\Delta - a^2 \sin^2 \theta} \right) \frac{\Sigma \sin^2 \theta d\phi^2}{(\Delta - a^2 \sin^2 \theta)}, \\ N_i dx^i &= - \frac{2m(r)ar \sin^2 \theta}{\Delta - a^2 \sin^2 \theta} d\phi. \end{aligned} \quad (52)$$

Optical (or spatial) metric defined in this way gives the arc length ($l = \gamma_{ij} dx^i dx^j$), where l is the affine parameter along the light curve [43]. The deflection angle α_D defined in Eq. (50) has contribution from the curvature of surface of light propagation $(^3)\mathcal{M}$ and the geodesics curvature of light curves as well. The Gaussian curvature of the surface is defined as [44]

$$\begin{aligned} K &= \frac{{}^3R_{r\phi r\phi}}{\gamma}, \\ &= \frac{1}{\sqrt{\gamma}} \left(\frac{\partial}{\partial \phi} \left(\frac{\sqrt{\gamma}}{\gamma_{rr}} ({}^3)\Gamma_{rr}^\phi \right) - \frac{\partial}{\partial r} \left(\frac{\sqrt{\gamma}}{\gamma_{rr}} ({}^3)\Gamma_{r\phi}^\phi \right) \right) \end{aligned} \quad (53)$$

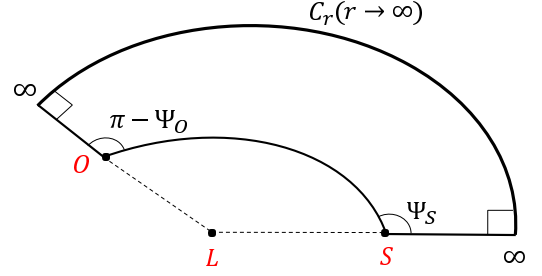


FIG. 10: Schematic figure for the quadrilateral $\infty\Box_S^\infty$ embedded in the curved space. The light emitted by the source S gets deflected by the black hole L and reaches the observer O .

where $\gamma = \det(\gamma_{ij})$. For a generic rotating and axially symmetric metric Eq. (3), the Gaussian curvature K is computed as

$$\begin{aligned} K &= \frac{-1}{6r^5(r-2m(r))} \left(6r^2(r-2m(r))(\Delta+a^2)m''(r) \right. \\ &\quad \left. + 6rm'(r)(rm'(r)-m(r))(\Delta+5a^2) + 6rm(r)^2 \right. \\ &\quad \left. - (7r^2+a^2)m(r) + 2r(r^2+3a^2) \right), \end{aligned} \quad (54)$$

using the Kalb-Ramond black hole mass function defined in Eq. (42) and considering a special case of $s = 1$, Eq. (54) yields

$$\begin{aligned} K &= \frac{3\Gamma}{r^4} + \frac{2\Gamma^2}{r^6} + \frac{8\Gamma a^2}{r^6} - \frac{3\Gamma^3}{2r^8} - \frac{6\Gamma^2 a^2}{r^8} - \left(\frac{2}{r^3} + \frac{6\Gamma}{r^5} \right. \\ &\quad \left. + \frac{6a^2}{r^5} - \frac{12\Gamma a^2}{r^7} + \frac{7\Gamma^2}{r^7} \right) M + \left(\frac{3}{r^4} - \frac{6a^2}{r^6} - \frac{10\Gamma}{r^6} \right) M^2 \\ &\quad + \left(\frac{4}{r^5} - \frac{6\Gamma}{r^7} \right) M^3 + \frac{2M^4}{r^6} + \mathcal{O}\left(\frac{M^5}{r^7}\right). \end{aligned} \quad (55)$$

A fully consistent analytic treatment of the metric Eq. (3) will involve an expansion in the powers of $(1/r)$, which will lead to very complicated expression. We exclusively work in the weak-field limit ensuring that it capture all the effects of the Kalb-Ramond field and consider only the leading order contributing terms. The surface integral of Gaussian curvature over the closed quadrilateral $\infty\Box_S^\infty$ reads [42]

$$\int \int_{\infty\Box_S^\infty} K dS = \int_{\phi_S}^{\phi_O} \int_{\infty}^{r_0} K \sqrt{\gamma} dr d\phi, \quad (56)$$

where r_0 is the distance of closest approach to the black hole. The boundary of integration domain, namely the curve from S to O in the quadrilateral $\infty\Box_S^\infty$, is unknown *a priori*, hence we first obtain the light orbit equation using Eqs. (29) and (31), that reads

$$\left(\frac{du}{d\phi} \right)^2 = F(u), \quad (57)$$

with

$$F(u) = \frac{u^4 \Delta^2 \left(((1 + a^2 u^2) - ab)^2 - \Delta u^4 (a - b)^2 \right)}{\left(a((1 + a^2 u^2) - ab) - \Delta u^4 (a - b) \right)^2}, \quad (58)$$

where $u = 1/r$, and $b \equiv \xi$ is the impact parameter. In the weak field approximation, we obtain the solution $u =$

$(\sin \phi)/b + \mathcal{O}(M, M^2)$ [42], and the integral Eq. (56) can be recast as

$$\int \int_{\infty \square \infty} K dS = \int_{\phi_S}^{\phi_O} \int_0^{\frac{\sin \phi}{b}} -\frac{K \sqrt{\gamma}}{u^2} du d\phi, \quad (59)$$

which for the rotating metric Eq. (52) reads as

$$\begin{aligned} \int \int K dS &= (\cos^{-1} b u_o + \cos^{-1} b u_s) \left(-\frac{3\Gamma}{4b^2} - \frac{3\Gamma a^2}{4b^4} + \frac{15\Gamma^2}{64b^4} - \frac{15M^2}{4b^2} - \frac{9M^2 a^2}{4b^4} + \frac{129M^2 \Gamma}{32b^4} + \frac{1355M^2 \Gamma^2}{256b^6} \right) \\ &+ \left(\sqrt{1 - b^2 u_o^2} + \sqrt{1 - b^2 u_s^2} \right) \left(\frac{2M}{b} + \frac{4Ma^2}{3b^3} - \frac{16M\Gamma}{3b^3} - \frac{24M\Gamma a^2}{5b^5} + \frac{40M^3}{9b^3} + \frac{168M^3 a^2}{25b^5} \right) \\ &+ \left(u_o \sqrt{1 - b^2 u_o^2} + u_s \sqrt{1 - b^2 u_s^2} \right) \left(-\frac{3\Gamma}{4b} - \frac{3\Gamma a^2}{4b^3} + \frac{15\Gamma^2}{64b^3} + \frac{5\Gamma^2 a^2}{8b^5} - \frac{M^2}{4b} + \frac{63M^2 \Gamma}{32b^3} - \frac{1355M^2 \Gamma^2}{256b^5} + \frac{9M^2 a^2}{4b^3} \right) \\ &+ \left(u_o^3 \sqrt{1 - b^2 u_o^2} + u_s^3 \sqrt{1 - b^2 u_s^2} \right) \left(-\frac{\Gamma a^2}{2b} + \frac{5\Gamma^2}{32b} + \frac{5\Gamma^2 a^2}{12b^3} - \frac{11\Gamma M^2}{16b} + \frac{3M^2 a^2}{2b} \right) \\ &+ \left(u_o^2 \sqrt{1 - b^2 u_o^2} + u_s^2 \sqrt{1 - b^2 u_s^2} \right) \left(\frac{M\Gamma}{3b} + \frac{2Ma^2}{3b} + \frac{17M\Gamma^2}{75b^3} - \frac{12M\Gamma a^2}{5b^3} + \frac{84M^3 a^2}{25b^3} - \frac{7M^3}{9b} + \frac{138M^3 \Gamma}{25b^3} \right) \\ &+ \mathcal{O} \left(\frac{M^2 a^2 \Gamma^2}{b^8}, \frac{M^4}{b^4} \right). \end{aligned} \quad (60)$$

Here, u_o and u_s are, respectively, the inverse of the r_o and r_s , the distances of observer and source from the black hole, and we have used $\cos \phi_o = -\sqrt{1 - b^2 u_o^2}$, $\cos \phi_s = \sqrt{1 - b^2 u_s^2}$. Interestingly, no linear term in a appear in Eq. (60), thus the contribution from the Gaussian curvature is insensitive to the direction of black hole rotation. Next, we calculate the geodesic curvature of the light curves, which is the surface-tangential component of the acceleration of the parameterized curve, and given by

$$k_g = -\frac{1}{\sqrt{\gamma \gamma^{\theta\theta}}} N_{\phi, r}. \quad (61)$$

For the metric (52), this reads

$$\begin{aligned} k_g &= -\frac{2Ma}{r^3} - \frac{2M^2 a}{r^4} + \frac{2a\Gamma}{r^4} - \frac{3M^3 a}{2r^5} + \frac{3Ma\Gamma}{r^5} \\ &- \frac{a\Gamma^2}{r^6} + \frac{3M^2 a\Gamma}{r^6} + \frac{66M^4 a}{r^6} \\ &+ \mathcal{O} \left(\frac{Ma\Gamma^2}{r^7}, \frac{M^3 a\Gamma}{r^7} \right) \end{aligned} \quad (62)$$

which identically vanishes for the non-rotating black hole. For the path integral of the k_g along the light curve, we consider a coordinate system centered at the black hole, and approximate the light curve as $r = b/\cos \vartheta$ and $l = b \tan \vartheta$ [42]. It is worthwhile to note that the geodesic curvatures of the curves from S to S_∞ and from O to O_∞ in Fig. 10 are both zero since these paths are geodesics. Whereas k_g is the geodesic curvature of the photon rays from S to O which is a spatial curve. This leads to

$$\begin{aligned}
\int_S^O k_g dl &= (\cos^{-1} bu_o + \cos^{-1} bu_s) \left(\frac{a\Gamma}{b^3} - \frac{aM^2}{b^3} - \frac{3a\Gamma^2}{8b^5} + \frac{9M^2 a\Gamma}{8b^5} \right) \\
&+ \left(\sqrt{1-b^2 u_o^2} + \sqrt{1-b^2 u_s^2} \right) \left(-\frac{2Ma}{b^2} + \frac{2Ma\Gamma}{b^4} - \frac{Ma\Gamma^2}{b^6} - \frac{M^3 a}{b^4} - \frac{88M^3 a\Gamma}{b^6} \right) \\
&+ \left(u_o \sqrt{1-b^2 u_o^2} + u_s \sqrt{1-b^2 u_s^2} \right) \left(\frac{a\Gamma}{b^2} - \frac{M^2 a}{b^2} - \frac{3a\Gamma^2}{8b^4} + \frac{15a\Gamma^3}{128b^6} + \frac{9M^2 a\Gamma}{8b^4} + \frac{1485M^2 a\Gamma^2}{32b^6} \right) \\
&+ \left(u_o^2 \sqrt{1-b^2 u_o^2} + u_s^2 \sqrt{1-b^2 u_s^2} \right) \left(\frac{Ma\Gamma}{b^2} - \frac{Ma\Gamma^2}{2b^4} - \frac{M^3 a}{2b^2} - \frac{44M^3 a\Gamma}{b^4} \right) \\
&+ \left(u_o^3 \sqrt{1-b^2 u_o^2} + u_s^3 \sqrt{1-b^2 u_s^2} \right) \left(-\frac{3a\Gamma^2}{4b^2} + \frac{5a\Gamma^3}{64b^4} + \frac{3M^2 a\Gamma}{4b^2} + \frac{495M^2 a\Gamma^2}{16b^4} \right) \\
&+ \left(u_o^4 \sqrt{1-b^2 u_o^2} + u_s^4 \sqrt{1-b^2 u_s^2} \right) \left(-\frac{3Ma\Gamma^2}{8b^2} - \frac{33M^3 a\Gamma}{b^2} \right) \\
&+ \left(u_o^5 \sqrt{1-b^2 u_o^2} + u_s^5 \sqrt{1-b^2 u_s^2} \right) \left(\frac{a\Gamma^3}{16b^2} + \frac{99M^2 a\Gamma^2}{4b^2} \right) + \mathcal{O} \left(\frac{M^2 a^2 \Gamma^2}{b^8}, \frac{M^4}{b^4} \right). \tag{63}
\end{aligned}$$

Here, we have assumed that $dl > 0$ such that the orbital angular momentum of the photons is aligned along the black hole spin, for otherwise case, $dl < 0$ can be taken which will leads to an extra -ve sign in Eq. (63). Using Eqs. (60) and (63) in Eq. (50), we obtain the analytical expression for the gravitational deflection angle of light in the rotating Kalb-Ramond black hole spacetime Eq. (3), which leads to very lengthy expression. Nevertheless, in the asymptotic limits, $u_o \rightarrow 0$ and $u_s \rightarrow 0$, the deflection angle for the rotating Kalb-Ramond black hole takes rather simpler form as follow

$$\begin{aligned}
\alpha_D &= \alpha_D|_{\text{Kerr}} + \left(-\frac{3\pi}{4b^2} + \frac{a\pi}{b^3} - \frac{3\pi a^2}{4b^4} + \frac{15\pi\Gamma}{64b^4} - \frac{3\pi a\Gamma}{8b^5} \right) \\
&+ \left(\frac{5\pi a^2 \Gamma}{8b^6} + \frac{15\pi a\Gamma^2}{128b^7} \right) \Gamma + \left(-\frac{32}{3b^3} + \frac{4a}{b^4} - \frac{48a^2}{5b^5} \right) \\
&+ \left(\frac{68\Gamma}{75b^5} - \frac{2a\Gamma}{b^6} \right) M\Gamma + \left(-\frac{129\pi}{32b^4} + \frac{9\pi a}{8b^5} - \frac{1355\pi\Gamma}{256b^6} \right) \\
&+ \left(\frac{1485\pi a\Gamma}{32b^7} \right) M^2\Gamma + \left(\frac{552}{25b^5} - \frac{176a}{b^6} \right) M^3\Gamma \\
&+ \frac{135\pi a}{8b^7} M^4\Gamma + \mathcal{O} \left(\frac{M^5 a}{b^6}, \frac{M^5 a\Gamma}{b^8} \right), \tag{64}
\end{aligned}$$

where $\alpha_D|_{\text{Kerr}}$ is identified as the Kerr deflection angle and reads as [42]

$$\begin{aligned}
\alpha_D|_{\text{Kerr}} &= \left(\frac{4}{b} - \frac{4a}{b^2} + \frac{8a^2}{3b^3} \right) M + \left(\frac{15\pi}{4b^2} - \frac{a\pi}{b^3} \right) \\
&+ \left(\frac{9\pi a^2}{4b^4} \right) M^2 + \left(-\frac{2a}{b^4} + \frac{80}{9b^3} + \frac{336a^2}{25b^5} \right) M^3 \\
&+ \left(\frac{21\pi}{64b^4} + \frac{99\pi a}{4b^5} \right) M^4 - \frac{96a}{5b^6} M^5 \\
&+ \mathcal{O} \left(\frac{M^6}{b^6}, \frac{M^6 a}{b^7} \right). \tag{65}
\end{aligned}$$

The deflection angle for the nonrotating Kalb-Ramond black hole can be obtained as a special case of $a = 0$

Γ	$a = 0.1$	$a = 0.3$	$a = 0.5$	$a = 0.7$	$a = 0.9$
0.1	0.0486188	0.0486058	0.0485929	0.04858	0.0485671
0.3	0.145856	0.145818	0.145779	0.14574	0.145701
0.5	0.243094	0.243029	0.242965	0.2429	0.242835
0.7	0.340331	0.340241	0.34015	0.34006	0.33997
0.9	0.437569	0.437452	0.437336	0.43722	0.437104
1.1	0.534806	0.534664	0.534522	0.53438	0.534238

TABLE I: The corrections in the deflection angle $\delta\alpha_D = \alpha_D|_{\text{Kerr}} - \alpha_D$ for the Sgr A* with $b = 10^3 M$, $r_s = 10^5 M$, $s = 1$ and varying Γ and a ; $\delta\alpha_D$ is in units of as .

from Eq. (64)

$$\begin{aligned}
\alpha_D &= \left(-\frac{3\pi\Gamma}{4b^2} + \frac{15\pi\Gamma^2}{64b^4} \right) + \left(\frac{4}{b} - \frac{32\Gamma}{3b^3} + \frac{68\Gamma^2}{75b^5} \right) M \\
&+ \left(\frac{15\pi}{4b^2} - \frac{129\pi\Gamma}{32b^4} - \frac{1355\pi\Gamma^2}{256b^6} \right) M^2 \\
&+ \left(\frac{80}{9b^3} + \frac{552\Gamma}{25b^5} \right) M^3 + \frac{21\pi}{64b^4} M^4 + \mathcal{O} \left(\frac{M^5}{b^5} \right) \tag{66}
\end{aligned}$$

which further reverts the value for the Schwarzschild black hole in the limiting case of $\Gamma = 0$ [45] as

$$\alpha_D|_{\text{Schw}} = \frac{4M}{b} + \frac{15\pi M^2}{4b^2} + \frac{80M^3}{9b^3} + \frac{21\pi M^4}{64b^4} + \mathcal{O} \left(\frac{M^5}{b^5} \right). \tag{67}$$

Setting up the premises for the gravitational lensing, next we discuss the possible astronomical implications of the rotating black holes in the presence of Kalb-Ramond field background. We aim to compare the lensing predictions of the rotating Kalb-Ramond black hole (3) with those for the Kerr and Schwarzschild black holes. We consider that the light coming from a distant source gets deflected from the Sgr A* black hole at the galactic center ($M = 4.6 \times 10^6 M_\odot$, $d = 8.3$ kpc) and reached the observer at the Earth. In this case, the observer distance d is much larger than the impact

Γ	$a = 0.1$	$a = 0.3$	$a = 0.5$	$a = 0.7$	$a = 0.9$
0.1	0.130854	0.295279	0.45966	0.623997	0.78829
0.3	0.228092	0.392491	0.556846	0.721157	0.885424
0.5	0.325329	0.489702	0.654032	0.818317	0.982558
0.7	0.422567	0.586914	0.751217	0.915477	1.07969
0.9	0.519804	0.684126	0.848403	1.01264	1.17683
1.1	0.617042	0.781337	0.945589	1.1098	1.27396

TABLE II: The corrections in the deflection angle $\delta\alpha_D = \alpha_D|_{\text{Schw}} - \alpha_D$ for the Sgr A* with $b = 10^3 M$, $r_s = 10^5 M$ and $s = 1$; $\delta\alpha_D$ is in units of as .

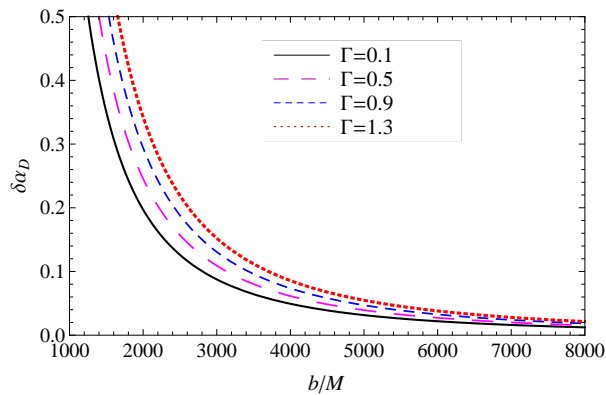


FIG. 11: Correction in the deflection angle $\delta\alpha_D = \alpha_D|_{\text{Kerr}} - \alpha_D$ for rotating Kalb-Ramond black hole with $s = 1$, $a = 0.5$ and varying b .

parameter of light, whereas a source star may live in the bulge of our Galaxy. Therefore, even though the source can be still in the weak field regime, we have to take account of finite-distance corrections that we have discussed in the paper. We calculate the light deflection angle and estimate the corrections from the Schwarzschild ($a = \Gamma = s = 0$) and the Kerr ($s = 0$) black holes. Tables I and II summarize these corrections, respectively, $\delta\alpha_D = \alpha_D|_{\text{Kerr}} - \alpha_D$ and $\delta\alpha_D = \alpha_D|_{\text{Schw}} - \alpha_D$, in deflection angle for various values of black hole parameters and $r_o = \infty$ and $r_s = 10^5 M$. One could see from Tables I and II that the presence of the Kalb-Ramond field significantly lower the deflection angle as compared to that for the Schwarzschild or Kerr black holes, and the order of correction is as which is within the resolution of today's observational facilities. The Kalb-Ramond field parameter Γ gets non-trivially coupled with the black hole rotation parameter a , such that for fixed values of Γ and b the correction in deflection angle from the Kerr black hole decrease with increasing a (cf. Table I). Nevertheless, α_D increases with increasing Γ and non-rotating black hole cause larger deflection angle as compared to the rotating one. This is because in the rotating spacetimes, the local inertial frame dragged along the black hole rotation, and it takes a shorter time for the light ray to feels the gravitational pull. In Fig. 11, we have shown how the difference in the deflection angle

$\delta\alpha_D = \alpha_D|_{\text{Kerr}} - \alpha_D$ vary with dimensionless impact parameter b/M for different values of Γ . As the impact parameter b increases, the correction in the deflection angle due to the Kalb-Ramond field get subside.

VI. CONCLUSION

The detection of the Kalb-Ramond field, which appears as closed string excitations in the heterotic string spectrum, may provide profound insights to our understanding of the current Universe [1, 9, 10]. The gravity when non-minimally coupled to the Kalb-Ramond field admits spherically symmetric hairy black holes [12]. We derived the rotating counterpart of this solution, i.e., rotating Kalb-Ramond black hole. The derived Kerr-like black hole has an additional Kalb-Ramond parameter s besides mass M and spin parameters a . The Kalb-Ramond field produces a hair that changes the structure of the rotating black hole through an extra term in metric (3). Obviously, this rotating Kalb-Ramond black hole metric is asymptotically flat and encompasses Kerr ($s = 0$), Kerr-Newman ($s = 1$), Reissner-Norstrom ($s = 1, a = 0$), and Schwarzschild ($s = 0, a = 0$) black holes. The rotating Kalb-Ramond black hole, like Kerr black hole, still admits the Cauchy and event horizons, as well as the SLS. However, the radii of horizons and SLS decrease due to s , and the ergosphere is also effected, thereby can have interesting consequences on the astrophysical Penrose process.

Despite the complicated rotating metric (3), using the Komar prescription, we analytically derived the exact expressions for conserved mass M_{eff} and angular momentum J_{eff} , valid at any radial distance. Further, the presence of the Kalb-Ramond field significantly altered these conserved quantities as compared to those for the Kerr black hole, which is restored in the limit $s = 0$; M_{eff} and J_{eff} decrease with increasing Γ or s for fixed values of other parameters. Nevertheless, the effect of the Kalb-Ramond field gets subsided at far distances from the horizon, as at asymptotically large r ($r \rightarrow \infty$) M_{eff} and J_{eff} take the values for the Kerr black hole. We further calculate the conserved quantity attributing to the generator of the event horizon to derive an interesting and important feature of the rotating black hole, namely the generalized Smarr formula.

Considering the observer and the source at the finite distance from the black hole, the analytical expression for the deflection angle in the weak-field limit is deduced and also the higher-order correction terms to the deflection angle for the Schwarzschild and Kerr black holes due to the Kalb-Ramond field are calculated. We illustrated that the presence of the Kalb-Ramond field leads to the smaller deflection angle as compared to Kerr and Schwarzschild black holes values. This change in the deflection angle, for the supermassive black hole Sgr A* and the light coming from the star source in the

bulge of Galaxy, is as large as a few arcseconds, thus feasibly measurable with the present-day astronomical observations. For fixed values of black hole parameters (M, Γ, s) and impact parameter b , non-rotating Kalb-Ramond black holes are found to cause a larger deflection angle in contrast to the rotating black holes.

We also discussed the effects of the Kalb-Ramond field on the black hole shadows, an extreme case of gravitational lensing. It is found that the shadows of rotating Kalb-Ramond black holes become smaller and more distorted with increasing field parameter s . The shadow observables, namely area A and oblateness D are used to characterize the size and shape of the shadows and thus in turn to extract the values of black hole parameters. The recent shadow observational results of M87* black hole are used to put constraints on the Kalb-Ramond field parameter in the supermassive black hole context. More severe constraints can be expected by taking into accounts the surrounding accretion disk.

The study of energy extraction and particle production rate in the rotating Kalb-Ramond black hole spacetime are being considered for future projects. It will also be interesting to investigate the stability of obtained rotating solution against the scalar perturbations in context of the gravitational wave observational data.

Acknowledgments

S.G.G. would like to thank DST INDO-SA bilateral project DST/INT/South Africa/P-06/2016 and also IUCAA, Pune for the hospitality while this work was being done. R.K. would like to thank UGC for providing SRF. A.W. thanks the staff at ZJUT for its hospitality, at which part of the work was done and also thanks the National Natural Science Foundation of China for partial support with Grant No. 11375153 and No. 11675145.

-
- [1] M. Kalb and P. Ramond, *Phys. Rev. D* **9**, 2273 (1974).
 [2] B. Altschul, Q. G. Bailey and V. A. Kostelecky, *Phys. Rev. D* **81**, 065028 (2010).
 [3] V. A. Kostelecky and S. Samuel, *Phys. Rev. Lett.* **63**, 224 (1989); K. Higashijima and N. Yokoi, *Phys. Rev. D* **64**, 025004 (2001); C. A. Hernaski, *Phys. Rev. D* **94**, 105004 (2016).
 [4] P. Majumdar and S. SenGupta, *Class. Quant. Grav.* **16**, L89 (1999).
 [5] P. S. Letelier, *Class. Quant. Grav.* **12**, 471 (1995).
 [6] D. Maity, P. Majumdar and S. SenGupta, *JCAP* **0406**, 005 (2004).
 [7] J. Ellis, N. E. Mavromatos and S. Sarkar, *Phys. Lett. B* **725**, 407 (2013); M. de Cesare, N. E. Mavromatos and S. Sarkar, *Eur. Phys. J. C* **75**, 514 (2015).
 [8] M. D. Seifert, *Phys. Rev. Lett.* **105**, 201601 (2010); P. H. Cox, B. C. Harms and S. Hou, *Phys. Rev. D* **93**, 044014 (2016); W. F. Kao, W. B. Dai, S. Y. Wang, T. K. Chyi and S. Y. Lin, *Phys. Rev. D* **53**, 2244 (1996); J. Erdmenger, R. Meyer and J. P. Shock, *JHEP* **0712**, 091 (2007); X. z. Li, P. Xi and Q. Zhang, *Phys. Rev. D* **85**, 085030 (2012); S. Kar, P. Majumdar, S. SenGupta and S. Sur, *Class. Quant. Grav.* **19**, 677 (2002).
 [9] S. Chakraborty and S. SenGupta, *JCAP* **1707**, 045 (2017).
 [10] S. Kar, S. SenGupta and S. Sur, *Phys. Rev. D* **67**, 044005 (2003).
 [11] I. Banerjee, B. Mandal and S. SenGupta, *JCAP* **1803**, 039 (2018).
 [12] L. A. Lessa, J. E. G. Silva, R. V. Maluf and C. A. S. Almeida, arXiv:1911.10296 [gr-qc].
 [13] R. P. Kerr, *Phys. Rev. Lett.* **11**, 237 (1963).
 [14] K. Akiyama *et al.*, *Astrophys. J.* **875**, L1 (2019).
 [15] K. Akiyama *et al.*, *Astrophys. J.* **875**, L6 (2019).
 [16] E. T. Newman, R. Couch, K. Chinnapared, A. Exton, A. Prakash and R. Torrence, *J. Math. Phys.* **6**, 918 (1965).
 [17] S. W. Hawking, *Commun. Math. Phys.* **25**, 152 (1972).
 [18] E. Poisson, *A Relativist's Toolkit: The Mathematics of Black-Hole Mechanics* (Cambridge University Press: Cambridge, UK, 2004).
 [19] S. Chandrasekhar, *The Mathematical Theory of Black Holes* (Oxford University Press, New York, 1992).
 [20] A. Komar, *Phys. Rev.* **113**, 934 (1959).
 [21] R. M. Wald, *General Relativity* (University of Chicago Press, Chicago (1984)).
 [22] S. K. Modak and S. Samanta, *Int. J. Theor. Phys.* **51**, 1416 (2012).
 [23] L. Smarr, *Phys. Rev. Lett.* **30**, 71 (1973).
 [24] J. M. Bardeen, B. Carter and S. W. Hawking, *Commun. Math. Phys.* **31**, 161 (1973).
 [25] J. L. Synge, *Mon. Not. R. Astron. Soc.* **131**, 463 (1966).
 [26] J. P. Luminet, *Astron. Astrophys.* **75**, 228 (1979).
 [27] J. M. Bardeen, *Black Holes*, Edited by C. DeWitt and B. S. DeWitt (Gordon and Breach, New York, 1973, p. 215).
 [28] C. T. Cunningham, J. M. Bardeen, *Astrophys. J.* **173**, L137 (1972).
 [29] A. de Vries, *Class. Quant. Grav.* **17**, 123 (2000); Z. Q. Shen, K.Y. Lo, M. C. Liang, P. T. P. Ho and J. H. Zhao, *Nature* **438**, 62 (2005); L. Amarilla, E. F. Eiroa and G. Giribet, *Phys. Rev. D* **81**, 124045 (2010); L. Amarilla and E. F. Eiroa, *Phys. Rev. D* **85**, 064019 (2012); L. Amarilla and E. F. Eiroa, *Phys. Rev. D* **87**, 044057 (2013); A. Yumoto, D. Nitta, T. Chiba and N. Sugiyama, *Phys. Rev. D* **86**, 103001 (2012); F. Atamurotov, A. Abdujabbarov, and B. Ahmedov, *Phys. Rev. D* **88**, 064004 (2013); A. Abdujabbarov, M. Amir, B. Ahmedov and S. G. Ghosh, *Phys. Rev. D* **93**, 104004 (2016); M. Amir, B. P. Singh and S. G. Ghosh, *Eur. Phys. J. C* **78**, 399 (2018).
 [30] A. Grenzebach, V. Perlick, and C. Lämmerzahl, *Phys. Rev. D* **89**, 124004 (2014); A. A. Abdujabbarov, L. Rezzolla, and B. J. Ahmedov, *Mon. Not. R. Astron. Soc.* **454**, 2423 (2015); P. V. P. Cunha and C. A. R. Herdeiro, *Gen. Rel. Grav.* **50**, 42 (2018); Y. Mizuno *et al.*, *Nat. Astron.* **2**, 585 (2018); R. Shaikh, *Phys. Rev. D* **100**, 024028 (2019); A. K. Mishra,

- S. Chakraborty and S. Sarkar, Phys. Rev. D **99**, 104080 (2019).
- [31] K. Beckwith and C. Done, Mon. Not. Roy. Astron. Soc. **359**, 1217 (2005).
- [32] T. Johannsen and D. Psaltis, Astrophys. J. **718**, 446 (2010).
- [33] T. Johannsen, Astrophys. J. **777**, 170 (2013).
- [34] B. Carter, Phys. Rev. D **174**, 1559 (1968).
- [35] R. Kumar and S. G. Ghosh, arXiv:1811.01260 [gr-qc].
- [36] O. Y. Tsupko, Phys. Rev. D **95**, 104058 (2017).
- [37] <https://eventhorizontelescope.org/>
- [38] C. Bambi, K. Freese, S. Vagnozzi and L. Visinelli, Phys. Rev. D **100**, 044057 (2019); I. Banerjee, S. Chakraborty and S. SenGupta, arXiv:1909.09385 [gr-qc]; R. Kumar, S. G. Ghosh and A. Wang, Phys. Rev. D **100**, 124024 (2019); R. Kumar, B. P. Singh and S. G. Ghosh, arXiv:1904.07652 [gr-qc]; I. Banerjee, S. Sau and S. SenGupta, arXiv:1911.05385 [gr-qc]; P. V. P. Cunha, C. A. R. Herdeiro and E. Radu, arXiv:1909.08039 [gr-qc].
- [39] G. W. Gibbons and M. C. Werner, Class. Quant. Grav. **25**, 235009 (2008).
- [40] M. P. Do Carmo, *Differential Geometry of Curves and Surfaces*, (Prentice-Hall, New Jersey, 1976).
- [41] A. Ishihara, Y. Suzuki, T. Ono, T. Kitamura and H. Asada, Phys. Rev. D **94**, 084015 (2016); A. Ishihara, Y. Suzuki, T. Ono and H. Asada, Phys. Rev. D **95**, 044017 (2017).
- [42] T. Ono, A. Ishihara and H. Asada, Phys. Rev. D **96**, 104037 (2017).
- [43] H. Asada and M. Kasai, Prog. Theor. Phys. **104**, 95 (2000).
- [44] M. C. Werner, Gen. Rel. Grav. **44**, 3047 (2012).
- [45] K. S. Virbhadra and G. F. R. Ellis, Phys. Rev. D **62**, 084003 (2000).